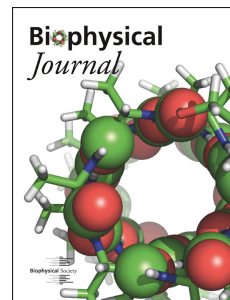


Journal Pre-proof

Integrin Mechanosensing relies on Pivot-clip Mechanism to Reinforce Cell Adhesion

Andre R. Montes, Anahi Barroso, Wei Wang, Grace D. O'Connell, Adrian B. Tepole, Mohammad R.K. Mofrad



PII: S0006-3495(24)00391-6

DOI: <https://doi.org/10.1016/j.bpj.2024.06.008>

Reference: BPJ 13101

To appear in: *Biophysical Journal*

Received Date: 13 December 2023

Accepted Date: 7 June 2024

Please cite this article as: Montes AR, Barroso A, Wang W, O'Connell GD, Tepole AB, Mofrad MRK, Integrin Mechanosensing relies on Pivot-clip Mechanism to Reinforce Cell Adhesion, *Biophysical Journal* (2024), doi: <https://doi.org/10.1016/j.bpj.2024.06.008>.

This is a PDF file of an article that has undergone enhancements after acceptance, such as the addition of a cover page and metadata, and formatting for readability, but it is not yet the definitive version of record. This version will undergo additional copyediting, typesetting and review before it is published in its final form, but we are providing this version to give early visibility of the article. Please note that, during the production process, errors may be discovered which could affect the content, and all legal disclaimers that apply to the journal pertain.

© 2024

1 Manuscript submitted to **Biophysical Journal**

2 **Article**

3 **Integrin Mechanosensing relies on Pivot-clip** 4 **Mechanism to Reinforce Cell Adhesion**

5 Andre R. Montes¹, Anahi Barroso¹, Wei Wang^{2,3}, Grace D. O'Connell³, Adrian B. Tepole^{*4}, and Mohammad R.K.
6 Mofrad^{*1,5}

7 ¹Molecular Cell Biomechanics Laboratory, Departments of Bioengineering and Mechanical Engineering, University of
8 California, Berkeley, California, 94720

9 ²Berkeley City College, Berkeley, California, 94704

10 ³Berkeley Biomechanics Laboratory, Department of Mechanical Engineering, University of California, Berkeley, California,
11 94720

12 ⁴Tepole Mechanics and Mechanobiology Laboratory, School of Mechanical Engineering, Purdue University, West Lafayette,
13 Indiana, 47907

14 ⁵Molecular Biophysics and Integrative Bioimaging Division, Lawrence Berkeley National Lab, Berkeley, California, 94720

15 *Correspondence: mofrad@berkeley.edu, abuganza@purdue.edu

16 **ABSTRACT** Cells intricately sense mechanical forces from their surroundings, driving biophysical and biochemical
17 activities. This mechanosensing phenomenon occurs at the cell-matrix interface, where mechanical forces resulting from
18 cellular motion, such as migration or matrix stretching, are exchanged through surface receptors, primarily integrins, and
19 their corresponding matrix ligands. A pivotal player in this interaction is the $\alpha_5\beta_1$ integrin and fibronectin (FN) bond, known
20 for its role in establishing cell adhesion sites for migration. However, upregulation of the $\alpha_5\beta_1$ -FN bond is associated with
21 uncontrolled cell metastasis. This bond operates through catch bond dynamics, wherein the bond lifetime paradoxically
22 increases with greater force. The mechanism sustaining the characteristic catch bond dynamics of $\alpha_5\beta_1$ -FN remains
23 unclear. Leveraging molecular dynamics simulations, our approach unveils a pivot-clip mechanism. Two key binding sites
24 on FN, namely the synergy site and the RGD (arg-gly-asp) motif, act as active points for structural changes in $\alpha_5\beta_1$
25 integrin. Conformational adaptations at these sites are induced by a series of hydrogen bond formations and breaks at the
26 synergy site. We disrupt these adaptations through a double mutation on FN, known to reduce cell adhesion. A whole-cell
27 finite element model is employed to elucidate how the synergy site may promote dynamic $\alpha_5\beta_1$ -FN binding, resisting cell
28 contraction. In summary, our study integrates molecular and cellular-level modeling to propose that FN's synergy site
29 reinforces cell adhesion through enhanced binding dynamics and a mechanosensitive pivot-clip mechanism. This work
30 sheds light on the interplay between mechanical forces and cell-matrix interactions, contributing to our understanding of
31 cellular behaviors in physiological and pathological contexts.

SIGNIFICANCE $\alpha_5\beta_1$ integrin serves as a mediator of cell-matrix adhesion and has garnered attention as a target
for impeding cancer metastasis. Despite its importance, the mechanism underlying the formation of a catch bond
between $\alpha_5\beta_1$ integrin and its primary ligand, fibronectin, has remained elusive. Our study aims to address this gap
by proposing a pivot-clip mechanism. This mechanism elucidates how $\alpha_5\beta_1$ integrin and fibronectin collaboratively
reinforce cell adhesion through conformational changes induced by the dynamic interaction of a key binding motif
known as the synergy site.

32 **INTRODUCTION**

33 Adhesion bonds enable cells to interact dynamically with their surrounding environment, orchestrating the regulation of essential
34 cellular processes such as proliferation, differentiation, and apoptosis (1–5). Integrins are transmembrane, heterodimeric
35 proteins that play an important role in cell adhesion by tethering the inside and outside of the cell via binding partners in
36 the extracellular matrix (ECM) (6). $\alpha_5\beta_1$ integrin is one of 24 integrin heterodimers present in mammals (4) and mediates
37 cell-tissue homeostasis by binding to its primary ligand, fibronectin (FN) (7, 8). $\alpha_5\beta_1$ and FN are linked together at the RGD
38 (Arg-Gly-Asp) motif and stabilized by the eight-amino-acid-long DRVPHSRN synergy site on FN (9), allowing extracellular

39 and cytoplasmic forces to be transmitted across the cell membrane. The accumulation of $\alpha_5\beta_1$ -FN bonds form the basis for
40 nascent cell adhesion and cell motion. Beyond $\alpha_5\beta_1$ -FN's role in maintaining cell-tissue homeostasis, it has been implicated as
41 a potential therapeutic target for cancer (10–12). For example, dysfunctional and overexpressed integrin bonds are markers of
42 uninhibited cancer cell migration (13, 14). As such, numerous antagonists have been developed to attenuate integrin bonds,
43 aiming to impede the invasion of multiple cancer cell types. Despite considerable efforts, these antagonists have faced challenges,
44 demonstrating limited success in effectively preventing cancer cell invasion. (15, 16). Therefore, a better understanding of the
45 biophysical nature of the $\alpha_5\beta_1$ -FN bond is needed to reveal mechanisms that can be exploited to target metastasis.

46 $\alpha_5\beta_1$ integrin creates a catch bond with FN (9, 17, 18), which is a type of bond that increases in lifetime with greater
47 applied force. The $\alpha_5\beta_1$ -FN catch bond allows for strong adhesion at the leading edge of a migrating cell and a steady release
48 of the bond at the cell's trailing end. Catch bonds have inspired development of synthetic catch bonds for manufacturing
49 resilient materials (19–21). However, the mechanisms involved in the $\alpha_5\beta_1$ -FN catch bond's ability to maintain its characteristic
50 strength is unknown. Understanding the underlying mechanism of $\alpha_5\beta_1$ -FN catch bond resilience could identify structural
51 protein characteristics that can be targeted to arrest cancer cells through substrate or protein modifications. Moreover, structural
52 dynamics that enable catch bond behavior may inspire development of resistant nanomaterials with self strengthening properties.

53 Ideally, the $\alpha_5\beta_1$ -FN catch bond could be imaged while an applied force is applied with a single-molecule testing setup
54 (e.g., optical trap or magnetic tweezers). However, current atomic-resolution molecular imaging techniques, like cryo-EM
55 and x-ray crystallography, require immobilizing the protein, making visualization of *in situ* structural changes of $\alpha_5\beta_1$ -FN
56 challenging. In light of these experimental limitations, molecular dynamics (MD) simulations have been used to visualize
57 protein conformational changes over time (22, 23).

58 Given $\alpha_5\beta_1$ -FN's critical role in mechanosensing via its elusive catch bond dynamics, we used MD simulations to visualize
59 the motion of $\alpha_5\beta_1$ -FN when acted on by an external load. We introduce a "pivot-clip" mechanism to model the $\alpha_5\beta_1$ -FN's
60 catch bond-like behavior, where the RGD motif acts as a stable pivot for FN about β_1 integrin and the synergy site acts as a
61 reinforcing clip connecting FN to α_5 . Past experiments demonstrated that mutating the synergy site diminishes catch bond
62 behavior and weakens whole-cell and single molecule adhesion to $\alpha_5\beta_1$ (18, 24). Even so, a lack of the synergy site does not
63 significantly limit cell traction on a 2D substrate under minimal contractility (25). To explain how the synergy site may promote
64 $\alpha_5\beta_1$ -FN binding while maintaining cell traction, we developed a 2D finite element (FE) model of the adhesive interface. Based
65 on our MD and FE models, we present a theory that the synergy site in FN reinforces cell adhesion via stronger binding affinity
66 and a mechanosensitive pivot-clip mechanism.

67 MATERIALS AND METHODS

68 Steered Molecular Dynamics Simulations

69 Constant velocity, all-atom steered MD simulations of the ectoplasmic $\alpha_5\beta_1$ -FN complex were run in GROMACS 2020.4 (26).
70 The 7NWL crystal structure file of the $\alpha_5\beta_1$ -FN complex with the TS2/16 Fv-clasp was downloaded from the protein data bank.
71 The $\alpha_5\beta_1$ integrin head domain and the FN type III fragment 7-10 were isolated using PyMOL (27). We used MODELLER
72 10.4 (28) to impose a virtual R1374/9A double mutation, switching the arginine residues in positions 1374 and 1379 in FN to
73 alanine (Figure 1B).

74 Wildtype and mutated structures were solvated in a TIP3P water box (18nm x 45nm x 19nm) with 0.15mM NaCl. Energy
75 was minimized for 15k steps with the steepest gradient descent algorithm, followed by an equilibration sequence of a 1ns NVT
76 simulation at 310K followed by a 10ns NPT simulation at 1 bar and 310K, per physiological conditions. Equilibration was
77 verified by ensuring that the RMSD of the fully unrestrained complexes (Figure S1) were within 0.3nm resolution of cryoEM.

78 The K559 and E36 residues at the proximal ends of the integrin headpieces were then restrained. P1142 at the distal
79 end of the FN fragment was pulled at 10 and 1nm/ns using a 50kJ/mol/nm spring with an umbrella potential for 3ns and
80 20ns, respectively. The steered MD simulations used a 2fs timestep. We visualized the crystal structures and MD simulation
81 trajectories using Visual Molecular Dynamics (VMD) 1.9.4a (29). All parameters for the MD simulations are available in the
82 supplementary materials (Table S1). The force and extension at $\alpha_5\beta_1$ -FN's center-of-mass (COM) were derived directly from
83 the output files from Gromacs. The extension was measured as the displacement of the $\alpha_5\beta_1$ -FN's center-of-mass with respect
84 to the first simulation frame. The radius of gyration of the α_5 and β_1 heads was measured using the built-in Gromacs function,
85 gmX gyrate. Distances between key bonds at R1374 and R1379 were calculated by averaging the distance between
86 atom pairs that could form hydrogen bonds using the VMD bond select and graph tool. We used a distance cutoff of 0.35nm
87 (3.5 Angstrom) and donor-hydrogen-acceptor angle cutoff of 30 in VMD to detect hydrogen bonds.

88 Synergy Site Departure Energy

89 To calculate the energy required for the synergy site to depart from α_5 , we used in-house Python code to integrate the force and
 90 COM extension data from the beginning of the simulation to the time of the force peak just before the rapid increase in extension
 91 rate. Since the force-extension data is non-monotonic, we first fitted a piece-wise linear function over the force-extension data
 92 before integrating with trapezoid rule.

93 Force Distribution Analysis

94 Time-resolved force distribution analysis (trFDA) was used to measure the punctual stresses based on the Coulombic interactions
 95 at all residues across all simulation time steps (30). The punctual stress is the absolute value of scalar pairwise forces exerted on
 96 each residue. Normally, stress would be in units of energy. However, the developers of punctual stress defined it as "force on
 97 a dimensionless point" which uses units of force (kJ/mol-nm). We opted to use this definition of punctual stress to remain
 98 consistent with past studies. Parameters for the trFDA are available in the supplementary materials (Table S2).

99 Long-term NPT Equilibration Simulations

100 Longer term stability of the $\alpha_5\beta_1$ -FN complex after synergy site mutagenesis was tested with two 250ns NPT simulations of
 101 $\alpha_5\beta_1$ -FN9-10: one wildtype and one R1374/9A mutant. The 7NWL pdb file was truncated from $\alpha_5\beta_1$ -FN7-10 to $\alpha_5\beta_1$ -FN9-10.
 102 A R1374/9A double mutation was again induced in silico via MODELLER 10.4 (28). The system contained ≈ 1.3 M atoms in a
 103 15nm x 30nm x 30nm box after solvation. NaCl concentration was kept at 0.15mM. The 250ns NPT simulation was preceded
 104 by a 15k step energy minimization and 1ns NVT as described previously. 100kJ/mol-nm² restraints were placed on residues
 105 D603, E445, and D1328 (Figure 4A) in the x and y directions, representing the remaining structures of integrin and FN while
 106 limiting periodic box crossing. No other restraints were placed. We used GROMACS 2020.4 (26) to measure backbone RMSDs,
 107 nonbonded energies, axes of inertia, distances, and hydrogen bonds. Axes of inertia were used to calculate angles by taking the
 108 inverse cosine of the dot product of a unit vector pair. Measurements were tested for normality with the Kolmogorov-Smirnov
 109 test. Since all data was non-normal, the wildtype and mutant trajectories were compared using the Wilcoxon signed rank test (α
 110 = 0.05).

111 Extensional Stiffness of α_5 and β_1 headpieces

112 Extensional stiffnesses of α_5 and β_1 headpieces were determined independently using 100ns NPT simulations. The 7NWL
 113 pdb file was isolated to either the α_5 head (≈ 438 K atoms in a 16.5nm x 16.5nm x 16.5nm box post solvation) or β_1 head (\approx
 114 463K atoms in a 16.8nm x 16.8nm x 16.8nm box post solvation). Again, energy minimization for 15k steps and a 1ns NVT as
 115 previously described were run in GROMACS prior to the 100ns NPT simulation. Extensional stiffness, k , for each molecule
 116 was calculated using:

$$k = \frac{k_B T}{\langle (L(t) - \langle L(t) \rangle_{\Delta t})^2 \rangle_{\Delta t}}, \quad (1)$$

117 where $k_B T$ is Boltzmann's constant, $T = 310$ K, $L(t)$ is the length of the reaction coordinate at time, t , and $\langle \rangle$ denotes the time
 118 average (31). For α_5 , the center-of-mass distance between D154 (synergy site binding residue) and D603 (connects to lower
 119 integrin legs) in α_5 was chosen as the length of the reaction coordinate. Similarly for β_1 , the Metal-Ion Dependent Adhesion
 120 Site (MIDAS; binds to RGD) and E445 (connects to lower integrin legs) were chosen. After the system had equilibrated, we
 121 used the latter 50ns for the extensional stiffness calculation. For each molecule, the distance data was divided into five 10ns
 122 blocks. Distances were saved every 10ps during the simulation, resulting in 1000 data points per block to calculate five k values
 123 per head. A Wilcoxon signed-rank test compared the means of the extensional stiffnesses of α_5 and β_1 . The angle between the
 124 propeller and thigh in α_5 was measured as described previously.

125 Whole-cell Finite Element Model

126 We used a whole-cell FE model to calculate the $\alpha_5\beta_1$ -FN concentration and force in a wildtype and mutant cell. We have
 127 previously modeled the cell-substrate interface using a whole-cell FE model; we refer the reader to that publication for the full
 128 set of model equations (23). In the present work, we introduced key changes to the catch bond model. We modeled the cell as a
 129 2D elastic disk with neo-Hookean constitutive material properties on a rigid substrate,

$$\sigma_c^{pas} = \mu_c \mathbf{b}_c - p_c \mathbf{I}, \quad (2)$$

Montes et al.

130 where σ_c^{pas} is the passive cell stress. The cell shear modulus is, $\mu_c=1\text{kPa}$ (32, 33). The deformation was characterized by the
131 left Cauchy-Green tensor \mathbf{b}_c . The pressure p_c was computed from plane stress boundary conditions.

132 An isotropic active stress field was applied inside the cell to model cell contractility,

$$\sigma_c^{\text{act}} = t_{\text{myo}} \mathbf{I}, \quad (3)$$

133 where σ_c^{act} is the active cell stress due to an actomyosin traction, t_{myo} in Pa (33, 34):

$$t_{\text{myo}} = \begin{cases} 100t & 0 < t < 2 \\ 200 & 2 \leq t \leq 30 \end{cases} \quad (4)$$

134 where t is the simulation time.

135 We used an existing catch bond model of adhesion to calculate the force-dependent concentration of $\alpha_5\beta_1$ -FN bonds per
136 node in the FE mesh (35–38). The catch model assumed that the $\alpha_5\beta_1$ -FN complexes behave as parallel springs that connect
137 and disconnect to the substrate based on an association constant, K_{on} and on a force dependent dissociation constant, K_{off} ,
138 respectively.

$$K_{\text{off}} = K_a e^{\frac{f_{\text{int}}}{F_a}} + K_b e^{-\frac{f_{\text{int}}}{F_b}}, \quad (5)$$

139 where K_a , F_a , K_b , and F_b are fitted parameters (Table S3) adapted from Bidone et al (38) and Takagi et al (39). f_{int} is the
140 magnitude of the force per $\alpha_5\beta_1$ -FN bond. The force vector per bond, (\mathbf{f}_{int}), is computed via the $\alpha_5\beta_1$ -FN spring constant
141 $k_{\text{int}} = 0.5\text{pN/nm}$ (17) and the spring extension vector \mathbf{u}_{int} :

$$\mathbf{f}_{\text{int}} = k_{\text{int}} \mathbf{u}_{\text{int}}. \quad (6)$$

142 The force per node, $\mathbf{f}_{i,\text{node}}$ is related to the dimensionless concentration of $\alpha_5\beta_1$ -FN bonds C with respect to the maximum
143 bond density $\rho_{i,\text{max}} = 100\mu\text{m}^2$ (40), and the local adhesion area A at that node,

$$\mathbf{f}_{i,\text{node}} = C \rho_{i,\text{max}} A \mathbf{f}_{\text{int}}. \quad (7)$$

144 At any node, i given the previous value of the bond concentration, C , the updated bond concentration $C_{t+\Delta t}$ at each progressive
145 time step is

$$C_{t+\Delta t} = C(1 - K_{\text{off}}\Delta t) + K_{\text{on}}\Delta t(1 - C). \quad (8)$$

146 Note that the updated eq. (8) is based on treating the bond kinetics in the limit of an ordinary differential equation discretized in
147 time with an explicit Euler scheme.

148 The internal force balance for the cell includes the elastic cell deformation (σ_c^{pas}) and the active cell contractile stress (σ_c^{act}):

$$\nabla \cdot \sigma_c + \mathbf{B} = \rho_c \mathbf{a}_c, \quad (9)$$

149 in which $\sigma_c = \sigma_c^{\text{pas}} + \sigma_c^{\text{act}}$ is the total cell stress, \mathbf{B} is the total body force on the cell, $\rho_c = 1000\text{kg/m}^3$ is the cell density (41)
150 and \mathbf{a}_c is the cell acceleration.

151 The strong form of the elastodynamic equation 9 has boundary conditions of the form $\sigma \cdot \mathbf{n} = \mathbf{t}$ on boundary Γ_c , which
152 includes the external forces on the circumference. Assuming 2D plane stress, the body forces on the cell arise from $\alpha_5\beta_1$ -FN
153 bond forces and viscous drag forces. The internal forces were computed through the weak form. Briefly, we multiplied equation
154 9 by test function, v , integrated over a domain Ω_c of thickness $1\mu\text{m}$, and applied divergence theorem to get the following weak
155 form for the cell.

$$-\int_{\Omega_c} \sigma_c : \delta \mathbf{d}_c \, d\Omega_c + \int_{\Gamma_c} \mathbf{t}_c \cdot \mathbf{v} \, dA_c + \int_{\Omega} \mathbf{v} \cdot \mathbf{B} = -\mathbf{R}_c + \mathbf{f}_{\text{circ}} + \mathbf{f}_{\text{body}} = \int_{\Omega_c} \rho \mathbf{a}_c \cdot \mathbf{v} \, d\Omega_c, \quad (10)$$

156 The $\delta \mathbf{d}_c$ is the variation of the symmetric velocity gradient, i.e. virtual work by moving each node by an independent variation
157 v . \mathbf{R}_c is the residual (internal forces) and the external force acting at a node of the cell mesh is composed of the forces on the
158 circumference, \mathbf{f}_{circ} and the forces on the body, \mathbf{f}_{body} :

$$\mathbf{f}_{\text{circ}} = \mathbf{f}_K + \mathbf{f}_{\text{ac}} + \mathbf{f}_A, \quad (11)$$

$$\mathbf{f}_{\text{body}} = \mathbf{f}_{i,\text{node}} + \mathbf{f}_d, \quad (12)$$

159 where $\mathbf{f}_{i,node}$ is the force due to $\alpha_5\beta_1$ -FN at each node, \mathbf{f}_d is viscous drag, \mathbf{f}_κ is curvature regularization, \mathbf{f}_{ac} is a random
160 fluctuation at the cell boundary from actin polymerization, and \mathbf{f}_A is an area penalty to counteract cell contractility.

161 The mesh was updated by a dynamic explicit mesh generator, El Topo (42), during the simulation run. The explicit mid-point
162 rule was used for time integration of the second order system of equations to update nodal velocities and positions. The
163 whole-cell FE simulation ran with a time step of $50\mu s$ over the course of an assigned time of $t_{sim} = 30s$. There were a total
164 of three simulation runs per R1374/9A mutant and wildtype catch bond condition, respectively. The three simulation bond
165 concentration and force outputs were time-averaged per condition.

166 RESULTS AND DISCUSSION

167 FN9- α_5 disengagement coincides with synergy site deactivation

168 We analyzed force-extension in conjunction with punctual stress to determine the role of the synergy site in FN9- α_5
169 disengagement. The initial force-extension curve of the wildtype $\alpha_5\beta_1$ -FN structure followed a linear response for both 10
170 and 1 nm/ns pull rates until peaking at 729pN and 462pN, respectively (Figure 2A and B). The peak forces coincided with
171 sharp decreases in the punctual stress at the synergy site, namely at sites R1374 and R1379 in FN9. R1379 has been shown to
172 be connected to D154 in the α_5 head via a salt bridge (13). However, R1374 has not been previously observed to be actively
173 linked to α_5 . At both pull rates, R1374 retained higher punctual stresses than R1379, but the sequence of disengagement was
174 dependent on the pull rate. Under the faster pull rate condition, the salt bridge was disrupted prior to a reduction in force on
175 $\alpha_5\beta_1$ -FN and punctual stress at R1374. This indicated that while the load on FN was sufficient to overcome the energetic barrier
176 to break the salt bridge connecting FN to α_5 , persistent electrostatic interaction at R1374 enabled FN9 to remain near the α_5
177 head. This was not observed under the slower pull rate simulation, where we noted simultaneous punctual stress reduction in
178 R1374 and R1379 at the peak force time point. While the punctual stresses at both residues were elevated during load ramping,
179 synergy site engagement reduced after the force peak.

180 R1374 and R1379 were contributors to punctual stress at the synergy site prior to the drop in force on $\alpha_5\beta_1$ -FN (Figure
181 S2). In both pull rate conditions, the combined punctual stress at R1374/9 prior to the force peak was on average two times
182 higher than other synergy site residues. Due to the high electrostatic activity of both sites prior to FN9 and α_5 separation, we
183 mutated both residues (R1374/9A) to evaluate their roles in maintaining $\alpha_5\beta_1$ -FN's structural response to force. At 10nm/ns,
184 the force response of the wildtype and mutant $\alpha_5\beta_1$ -FN were similar, peaking at 729pN and 704pN, respectively (Figure 2C).
185 However, the punctual stresses at A1374 and A1379 were 45% and 40% lower in the mutant case than the wildtype (Figure 2C
186 and D), indicating that the mutation disrupted synergy site engagement, but not necessarily reduced force transmission. Similar
187 trends were observed in the 1nm/ns force rate condition, where the punctual stresses at A1374 and A1349 were small relative to
188 R1374 and R1379, and the first peak force was lower in the mutant case (wildtype = 462pN, mutant = 291pN; Figure 2D).

189 Although our results appeared to conflict with the understanding that synergy site mutagenesis decreases cell adhesion
190 strength, the relative energetic barrier required to separate the synergy site from integrin revealed closer agreement with the
191 literature (17, 18, 24, 39, 43). While we noticed a 171pN difference (37% less than the wildtype) in the first peak force in
192 the 1nm/ns mutant model, we only noted a 25pN drop (3% less than the wildtype) in the 10nm/ns model. This is likely a
193 consequence of the high pull rates used in these models that may hide molecular mechanisms. Therefore, long term simulations
194 at slower pull rates and smaller forces are needed to overcome this limiting factor. We worked towards this goal in a later section.
195 For now, to overcome this potential conflict with the literature, we opted to use the area under the force-extension curve (Figure
196 S4) as a proxy for measuring synergy site departure energy, which would be related to the energy barrier required to pull FN9
197 away from α_5 . We defined the *synergy site departure force* as point (i) in all simulations (Figure 2). Forces recorded after the
198 *synergy site departure force* would work to unfold FN and unbind RGD. We found that the synergy site departure energies
199 were greater in the wildtype, in line with past in vitro experiments that show greater binding affinity of $\alpha_5\beta_1$ integrin to FN in
200 the presence of the synergy site (24, 39). At 10nm/ns, the wildtype and mutant energies were 4012pN-nm and 2715pN-nm,
201 respectively. At 1nm/ns, the wildtype and mutant had a energies of 1529pN-nm and 883pN-nm, respectively. These values do
202 not have any physical meaning, but enabled a comparison between the wildtype and mutant. From our current steered MD data,
203 we cannot make claims about the effect of the synergy site on RGD binding specifically. Free energy methods such as FEP (free
204 energy perturbation) and MMPBSA (Molecular Mechanics Poisson-Boltzmann Surface Area) would be more appropriate to
205 study these effects computationally and are the subject of ongoing work.

206 Punctual stress measurements provided insight into per-residue interactions at the synergy site and are substantiated by
207 atomic-level interactions. Specifically, the formation and breakage of hydrogen bonds between α_5 and FN9 are essential for
208 relaying force between the two. Since high punctual stresses were observed on R1374 and R1379, we tracked bonds between
209 R1379—D154 and R1374—E124 (Figure S5A). At both pull rates, the R1379—D154 salt bridge was broken before the
210 maximum force was reached, while residue R1374 remained bounded to either E124 or E81 depending on the pull rate (Figure

211 S5B-C). The measured distance between R1374—E124 was within the range of a hydrogen bond (0.35nm) after the departure of
 212 the R1379—D154 bond (10nm/ns case; Figure S5D). At the slower pull rate, R1374 transitioned from E124 to E81, maintaining
 213 contact between FN9 and $\alpha_5\beta_1$ together with R1379—D154 (Figure S5E). Both bonds then released and the force on $\alpha_5\beta_1$ -FN
 214 consequently dropped. The R1374/9A double mutation severed the main points of contact between FN9 and $\alpha_5\beta_1$, pushing the
 215 distance between the residues to 0.65nm, beyond the 0.35nm hydrogen bond length cutoff (Figure S5F).

216 For all test cases, the peak forces were followed by sharp increases in extension rate, suggesting a rapid conformational
 217 change of $\alpha_5\beta_1$ -FN (Figure 2). In the case of the wildtype 10nm/ns pull rate, the measured extension rate increased from
 218 5.10nm/ns to 14.4nm/ns. Similarly, the wildtype 1nm/ns pull rate increased in rate from 0.547nm/ns to 1.82nm/ns (Table S4).
 219 Notably, there was a mismatch between the input rate and measured rate. Steered MD simulations attempt to control the pull
 220 rate via a virtual spring connecting a dummy atom to the pulled site. While the atom moves at a constant rate, the molecule's
 221 response depends on the virtual spring deflection and local conformational changes associated with the molecule. Therefore, it
 222 is unlikely that the input pull rate matches the measured pull rate experienced by the molecule. Further, the output extension
 223 was measured as the distance traveled by $\alpha_5\beta_1$ -FN's COM, which depends on the structural behavior.

224 Our reported forces and pull rates are many orders of magnitude higher than what has been tested using atomic force
 225 microscopy (AFM; 1 - 15 $\mu\text{m/s}$) (43). Given our large 1.5M atom system, we compromised on the simulation time scale by
 226 applying extension rates within the bounds of past steered MD simulations of integrin (0.1 - 10 nm/ns) (22, 44). The fast
 227 extension rates contributed to simulated forces beyond what has previously been measured experimentally (single molecule
 228 rupture forces of 80-120pN) (43). Nevertheless, the difference between the forces generated at 1 and 10 nm/ns hinted at
 229 force-dependent behavior arising from synergy site engagement. Larger conformational changes were visually noted in the α_5
 230 head during 10nm/ns pulling compared to 1nm/ns pulling. Further, the mutants showed little to no changes in the movement
 231 of the α_5 head, suggesting that the interactions at the synergy site could work to deform α_5 . Therefore, we quantified the
 232 conformational changes associated with synergy site engagement when subjected to high pull rates.

233 Conformational response of α_5 and β_1 was hampered by lack of synergy site engagement

234 We informed the differences in force and extension rates across conditions by visualizing the structural changes of $\alpha_5\beta_1$ -FN
 235 under both pull rates for the wildtype and mutant cases. We used the radius of gyration to quantify conformational changes
 236 within α_5 and β_1 heads, with smaller radii indicating more compact proteins. In both wildtype runs, the α_5 head, which is
 237 connected to the synergy site on FN9, stretched further than the β_1 head, which is connected to the RGD motif on FN10.
 238 However, pull rate affected the degree of α_5 stretching. The lower 1nm/ns pull rate resulted in 0.165nm increase in α_5 's radius
 239 of gyration (Figure 3A), compared to a 0.407nm increase in the 10nm/ns rate simulation (Figure S3A). Most of the α_5 head
 240 deformation resulted before the peak force and synergy site disengagement. For the respective 10nm/ns and 1nm/ns rates,
 241 97.7% and 99.0% of the max α_5 head deformation occurred prior to the peak force, when the synergy site loosened. From
 242 the observations of $\alpha_5\beta_1$ -FN's quaternary structure, we noticed the α_5 head straightening while FN9 remained connected
 243 at the synergy site (Figure 3C). Further, at higher forces, α_5 underwent a greater degree of stretching while FN9 unfolded
 244 (Figure S3C). In contrast, lower forces seemed to encourage synergy site disengagement prior to FN unfolding. Our observation
 245 suggests that $\alpha_5\beta_1$ -FN's catch bond dynamics may be promoted by greater synergy site interaction in combination with α_5
 246 extension to resist larger forces. The greater interaction may stem from the hydrogen bond electrostatics at R1374 and R1379
 247 that bridge α_5 to FN9 (Figure S5).

248 We tested the degree to which the synergy site contributed to structural changes in $\alpha_5\beta_1$ -FN by mutating the site (R1374/9A)
 249 and again measuring the radius of gyration of α_5 and β_1 under an external load on FN. Surprisingly, the mutant pulled at
 250 10nm/ns still resulted in conformational changes of the α_5 head, with the radius of gyration increasing by 0.266nm. However,
 251 this was less than the 0.407nm increase observed in the wildtype (Figure S3B). Further, the mutant pulled at the slower 1nm/ns
 252 showed virtually no deformation of α_5 or β_1 (Figure 3B). Investigating the quaternary structure of the mutant revealed that FN9
 253 was separated immediately from α_5 (Figures 3D and S3D). As the FN beta sheets stacked vertically in alignment with the
 254 pulling direction, the force increased and peaked as soon as FN10 begun to unfold. For all simulations, the β_1 head kept a
 255 more stable conformation, maintaining its radius of gyration within 0.12nm. These results are indicative of a new mechanism
 256 whereby α_5 and FN deformation patterns may be altered due to interactions at the synergy site. However, the fast pull rates
 257 are five orders of magnitude higher than even the slowest AFM pull rates, posing the question of whether these states may be
 258 realized and more importantly, have a physical meaning. So, while our results were promising, we aimed to address the pull rate
 259 limitation by conducting longer term simulations and emphasizing our analysis on the synergy site and integrin interaction.

260 Synergy site interactions maintained FN9 and α_5 close

261 We used two 250ns NPT simulations of $\alpha_5\beta_1$ integrin in complex with FN9-10 (wildtype and R1374/9A) to understand the role
262 of the synergy site in maintaining integrin and FN conformational stability. Visual observation showed separation of mutant
263 FN9 away from integrin as well as minor deviations to the integrin headpieces (Figure 4B). Therefore, we investigated the
264 connection between FN9 and integrin. As expected, we found that the nonbonded interactions (van der Waals and coulombic
265 energies) between the synergy site and $\alpha_5\beta_1$ were greater in the wildtype structure (Figure 4C). These results aligned with the
266 shorter distance between R1379 in FN9 and D154 in α_5 (Figure 4D) as well as the greater number of hydrogen bonds between
267 the synergy site and α_5 (Figure S6A).

268 Lower synergy site engagement widened the gap between FN9 and α_5 , but only minor structural changes in the integrin
269 heads and FN were realized. We conducted structural analyses using the final 50ns of the 250ns simulation. The nonbonded
270 interactions (Figure 4A), the hydrogen bond count (Figure S6A), and backbone RMSD (Figure S6B) of $\alpha_5\beta_1$ -FN9-10 (wildtype
271 and mutant) leveled off at ≈ 200 ns, suggesting system equilibration. Longer simulations would be necessary to evaluate whether
272 the system fully equilibrated, but based on these initial trends, we enforced the latter 50ns cutoff. Since the synergy site in
273 FN9 and RGD in FN10 are two anchoring contact points for integrin, we posited that releasing FN9 from α_5 via synergy
274 site inhibition would increase FN9-10 flexibility. Interestingly, the means of the FN9-10 angles (θ_{FN}) in both cases was not
275 statistically significant and variance was greater in the wildtype (Figure 4E), which would indicate that the wildtype FN9-10
276 was fluctuating to a greater degree even as the synergy site was interacting more strongly. Further, the α_5 - β_1 angle (θ_{int}) in the
277 wildtype was 7.2° larger than the mutant, pointing to a modest closing of the integrin heads in the mutant (Figure 4F). This
278 closing was predominantly a result of FN9-10 rotation rather than a state transition of α_5 . The propeller-thigh angle (θ_{α_5}) was
279 4.7° greater in the mutant, whereas the β_1 -FN10 angle (θ_{β_1-FN10}) was 12.1° lower in the mutant (Figure S8). FN9-10 retained
280 its shape, with only a 0.01nm difference in radius of gyration between mutant and wildtype (Figure S7A-B). Additionally, there
281 was no statistically significant difference in the radius of gyration of α_5 between mutant and wildtype (Figure S7C-D). The
282 radius of gyration of β_1 in the mutant was 0.16nm smaller (Figure S7E-F), indicating a small amount of compression of β_1 as it
283 interacted with FN10. The time series data of θ_{FN} (Figure S6C), θ_{int} (Figure S6D), θ_{α_5} (Figure S8B), and θ_{β_1-FN10} (Figure
284 S8D) showed overlap between mutant and wildtype throughout the entire simulation, meaning that some states may be similar
285 to each other, but on average, the conformational measurements suggest that the synergy site locks FN9 to α_5 and prevents
286 rotation of FN9-10.

287 The unlocking of FN9 due to reduced synergy site energetics did not promote appreciable changes at integrin's RGD
288 binding location. We first measured the nonbonded interaction energies between RGD and $\alpha_5\beta_1$, including the MIDAS cation,
289 which showed no differences in energies after, and even before the imposed 200ns cutoff (Figure S9A). Additionally, the number
290 of hydrogen bonds between α_5 and RGD (Figure S9B) well as β_1 and RGD (Figure S9C) were similar between the wildtype
291 and mutant. From this data, we assumed that RGD would be a stable location for FN to maintain binding to integrin regardless
292 of synergy site engagement. To confirm the conformational stability at the RGD binding area, we measured the mean and
293 minimum distances between notable interactions at this site (Figure S10A). These included RGD-MIDAS (Figure S10B-C),
294 D227-RGD (Figure S10D-E), and S134-MIDAS (Figure S10F-G). As expected, the distances between these pairs remained
295 small in both the wildtype and mutant. Although there were differences in the S134-MIDAS mean and minimum distance, the
296 observed 0.05-0.75nm distance difference was not enough to decrease the absolute interaction energy at the mutant's RGD site
297 (Figure S9A). The stability of the RGD binding site enabled it to behave like a pivot point for mutated FN9-10 when FN9
298 dislodged from the synergy site. Since our data suggests that RGD remained stable regardless of synergy site engagement, we
299 reasoned that the additional synergy site interaction energies in the wildtype would only bolster $\alpha_5\beta_1$ -FN binding. From past *in*
300 *vitro* experiments, RGD alone is known to be sufficient to support some $\alpha_5\beta_1$ integrin binding and cell adhesion, though it has
301 been shown that the synergy site promotes longer lasting binding and stronger cell adhesion when it binds in tandem with RGD
302 to secure FN (6, 24). The synergy site alone does not support cell adhesion as well as only RGD, or both RGD and the synergy
303 site (45, 46), which may be attributed to the synergy site's lower nonbonded interaction energy (Figure 4C) compared to RGD
304 (Figure S9A). However, as mentioned, free energy methods must be considered to include the entropic effects that we do not
305 account for in this work.

306 Collectively, our observations of the 250ns NPT trajectories support the conjecture that the synergy site reinforces integrin
307 engagement with the matrix (13, 24). Further, our accelerated steered MD models imply that force between the synergy site and
308 α_5 integrin head may induce conformational changes of α_5 integrin. Overall, our results highlight the importance of the synergy
309 site clip in stabilizing and reinforcing the $\alpha_5\beta_1$ -FN bond after initial catch bond formation, which has also been previously
310 suggested experimentally (9, 25, 47, 48). While cell adhesion can be negated altogether by an RGD deletion as demonstrated by
311 spinning disk assays, the R1374/9A double mutation reduces cell adhesion strength by around 90% (24). So, while adhesion
312 could still occur, the bond strength was compromised due to the synergy site mutation, which has also been shown previously
313 through single molecule AFM (43). Additionally, past surface plasmon resonance binding assays measure an 11-fold decrease

314 in affinity between $\alpha_5\beta_1$ and R1374A FN compared to wildtype (39). Clearly, the role of the synergy site in maintaining a firm
 315 adhesion cannot be understated. Here, we propose how the synergy site may give rise to specific molecular states of $\alpha_5\beta_1$ -FN,
 316 since it holds FN9 near α_5 . Our steered MD models at a 1nm/ns pull rate showed a decrease in initial synergy site departure
 317 energy after mutagenesis, implying that there is a greater energetic barrier in breaking the synergy site than when it is inhibited.
 318 Further, the 1nm/ns wildtype model predicts that the connection between FN9- α_5 maintained by the synergy site could deform
 319 the α_5 head when loaded, which was not observed in the 1nm/ns mutant run. While our MD study highlighted the reinforcing
 320 role of the synergy site at the molecular scale, we also sought to explore how this adhesion reinforcement may dynamically
 321 manifest at the whole cell scale.

322 Synergy site presence led to adhesion reinforcement by recruiting $\alpha_5\beta_1$ integrin

323 We employed a whole-cell FE model that analyzed the adhesion interface that contained $\alpha_5\beta_1$ -FN bonds under an isotropic cell
 324 contraction that drove bond extension (Figure 5A). Our simple model demonstrated an adaptive reinforcement of collective
 325 $\alpha_5\beta_1$ -FN bonds due to the stronger binding affinity afforded by the synergy site. We modified the parameters for the $\alpha_5\beta_1$ -FN
 326 binding kinetics (Table S3) to produce bond lifetime curves for the wildtype bond and R1374/9A mutant (Figure 5B). The
 327 differences in parameters between the two bond types resulted in an 11-fold decrease in $\alpha_5\beta_1$ -FN bond concentration (Figure
 328 5C), but no increase in equilibrium force (Figure 5D). The areas of high concentrations and high forces are present at the
 329 periphery of the cell model during contraction (Figures 5E and 5F), which has been shown by 2D Fluorescence Resonance
 330 Energy Transfer (FRET) and traction force microscopy (TFM) assays (25). Notably, mutant bonds compensate for the lack of
 331 number of bonds by sustaining more of the cell's contractile load. The higher recruitment of wildtype bonds distributes the
 332 forces more evenly across the cell model.

333 Our whole-cell FE model sheds light on the dynamic force balance at short timescales that are not as apparent experimentally.
 334 TFM of cells plated on 2D substrates have shown that cell contraction and individual bond force were not altered due to an
 335 absence of the synergy site (25, 48). Our model used the same 200Pa cell contraction across both conditions, but showed a stark
 336 difference in how the adhesion forces are handled by the bonds. Namely, while forces eventually equalized between mutant and
 337 wildtype conditions, we observed an initial dynamic adjustment of high forces at the cell model's boundary for mutant bonds
 338 (Figure 5F). Specifically, average forces measured from mutated bonds peaked at 7pN, while wildtype bonds peaked at 3pN;
 339 both average bond forces were within the previously measured 1-7pN range (25). A body of work has shown the reduction in
 340 cell adhesion strength at the single molecule and whole cell scale due to a lack of synergy site engagement (24, 25, 43, 48). In
 341 spite of the reduced bond strength, our model showed that, under minimal tension, the binding affinity gain due to the presence
 342 of the synergy led to a more stable, dynamic force balance across the $\alpha_5\beta_1$ -FN bonds on the cell model's surface.

343 Pivot-clip mechanism of $\alpha_5\beta_1$ -FN as a model for cell adhesion reinforcement

344 The mechanosensitive pivot-clip mechanism provides a model to consider how the $\alpha_5\beta_1$ -FN catch bond reinforces cell adhesion
 345 across molecular and cell scales under cell-matrix forces (Figure 6). Long term NPT simulations indicated that role of the
 346 synergy site was to clip FN9 close to α_5 as evidenced by the increased separation between FN9 and α_5 in the mutant. The
 347 dislodging of FN9 did not modify the stability of the RGD site. In our steered MD simulations, for both pull rates tested in the
 348 wildtype $\alpha_5\beta_1$ -FN, the unbinding of FN9- α_5 coincided with a plateauing of α_5 extension (Figures 3A and S3A). With the link
 349 between FN9- α_5 broken, FN10 was free to rotate about the RGD motif on β_1 (Figures 3D and S3D). The FN10 rotation about
 350 the RGD site was maintained in the mutant steered MD runs while diminishing the increase in radius of gyration of α_5 (Figure
 351 S3B and D). Based on the structural changes observed on α_5 in the steered MD simulations, the synergy site clipped the α_5
 352 head to FN9 while the RGD motif on β_1 acted as a pivot for FN10 (Figure 6). Since α_5 preferentially stretched instead of β_1 , we
 353 conducted 100ns NPT simulations of each integrin head to measure each of their relative extensional stiffness. Upon confirming
 354 a stable RMSD after 50ns (Figure S11A), we averaged the measured α_5 and β_1 head distances over five 10ns blocks (Figure
 355 S11B) to quantify extensional stiffness. We measured extensional stiffnesses of 2587 pN/ μ m and 174548 pN/ μ m for the α_5
 356 and β_1 heads, respectively (Figure S11C). Based on the distance fluctuations, β_1 remained more static, while α_5 seemed to
 357 oscillate. We also found that the propeller-thigh angle of α_5 decreased (Figure S11D), giving α_5 a more bent shape (Figure
 358 S11E). We reasoned that the link between the propeller and thigh grants α_5 its flexibility to stretch when force is applied, while
 359 β_1 's rigidity could provide a route for forces to transmit towards cytoskeletal proteins. While it has been known that the synergy
 360 site plays a role in catch bond dynamics (17, 24), the clip engagement under force could be one mechanism by which the
 361 synergy site enables catch bond dynamics at the molecular scale. Using our pivot-clip model (Figure 6), forces generated at the
 362 cell-matrix interface would need to first overcome the synergy site clip energy barrier. In parallel, α_5 would resist forces by
 363 stretching prior to FN9 unclipping, also leading to a higher barrier than if the synergy site were not present. Additionally, the
 364 rigidity of β_1 could facilitate downstream mechanosignaling via talin. Namely, talin binds to the β_1 tail and has been shown to

365 be a mechanosensitive protein that interacts with vinculin and focal adhesion kinase to promote focal adhesion maturation
 366 and nuclear localization of transcriptional coregulator, Yes-Associated Protein (36, 49, 50). However, larger forces could also
 367 increase the probability of FN unbinding from $\alpha_5\beta_1$, especially when the additional energetic barrier from the synergy site
 368 is not present. Past assays have demonstrated that $\alpha_5\beta_1$ -FN unbinding occurs with greater likelihood when the synergy site
 369 is inhibited; moreover, $\alpha_5\beta_1$ -FN losing its catch bond characteristics (18, 24). To determine the exact pathway of the force
 370 transmission across the $\alpha_5\beta_1$ -FN catch bond with and without the synergy site, much longer and slower MD simulations are
 371 needed. Along those lines, more investigation is warranted to elucidate how the full structure of $\alpha_5\beta_1$ dynamically couples with
 372 mechanosensitive cytoskeletal proteins at the atomistic scale.

373 In the context of outside-in signaling, the $\alpha_5\beta_1$ -FN pivot-clip mechanism demonstrates how the synergy site could route
 374 force via β_1 towards mechanosignaling proteins in the cytoplasm, like talin, leading to integrin clustering. According to the
 375 outside-in activation model, integrins maintain a bent-closed, low affinity state before undergoing a conformational change to
 376 an extended, active conformation upon encountering an ECM ligand (Figure 1A) (51–53). In contrast, the inside-out model
 377 proposes that the adaptor protein talin would bind to the cytoplasmic tail of integrin, allowing it to activate and subsequently
 378 bind to its ligand (51–53). While the current hypothesis states that binding between FN and $\alpha_5\beta_1$ triggers an opening of
 379 integrin's cytoplasmic tails leading to an accumulation of adaptor proteins that resist cell-matrix forces (Figure 6), further
 380 studies are needed to elucidate the mechanism behind integrin activation. Multiple steered MD models have been employed to
 381 interrogate β_3 integrin activation (22, 44, 54–57), with few investigating the cytoplasmic end of β_1 integrin (58, 59). However,
 382 to our knowledge, our approach is unique in that we model the interface between FN and the $\alpha_5\beta_1$ integrin heads, where forces
 383 are transmitted bidirectionally between the cell and its matrix.

384 Our study acknowledges several limitations. Firstly, we made the assumption that the proximal ends of the integrin heads
 385 were anchored by fully extended integrin legs tightly held by tails in the cell membrane. While this assumption contributed to
 386 model stability, it is worth noting that the head-leg junction has been suggested to possess greater flexibility (13). Relaxing the
 387 constraints on the proximal ends to allow lateral movement may introduce flexibility without the added complexity of integrating
 388 the legs. Secondly, our steered MD models applied a large, vertical pulling rate. While this approach is advantageous for directly
 389 stressing the points of contact between FN and $\alpha_5\beta_1$, it could introduce biased pulling and rotational forces that are unrealistic,
 390 which would decrease model confidence. Multiple runs and a parametric study of boundary conditions must be considered
 391 when confirming our MD simulations in future works investigating tension or other loading modalities, such as shear or torsion.
 392 Lastly, our focus was on a specific integrin subtype. The intricate nature of cell-matrix interactions involves multiple integrin
 393 subtypes and their respective ligands. Due to the prohibitive cost of molecular dynamics simulations, alternative approaches
 394 such as coarse-grained or agent-based models, capable of examining cell-matrix interactions at a broader systems level and over
 395 extended timescales, may be necessary.

396 CONCLUSION

397 This work advances our understanding of cell mechanobiology by introducing a mechanosensitive mechanism, termed pivot-clip,
 398 by which $\alpha_5\beta_1$ integrin reinforces cell adhesion. Using FE and MD simulations, we shed light on a biophysical connection
 399 between the cell and ECM that underpins many cellular behaviors that drive physiology and pathology. Critically, we also
 400 demonstrated binding domains that promote catch bond dynamics in the context of cell-matrix mechanosensing. Looking
 401 forward, we envision elucidating how the force-dependent, pivot-clip mechanism interacts with its surrounding machinery
 402 and how it may be transformed via novel therapeutics. As our understanding of cell adhesion progresses, we aim to develop
 403 informed approaches to target diseases that rely on transmitting forces via cell-matrix bonds.

Figure 1: A) Schematics of $\alpha_5\beta_1$ integrin in its bent-closed, inactive state with FN fragment 7-10 unbound (left), extended-
 active state in complex with FN (middle), and under an applied load (right). B) The Cryo-EM structure of $\alpha_5\beta_1$ -FN with
 the individual integrin heads and FN fragments labeled. The MD simulations applied a velocity to the P1142 residue while
 restraining K559 and E36. Zoomed in region shows wildtype synergy site with R1374 and R1379 (left) and double mutated
 R1374/9A synergy site (right). D154 binds to R1379 and is shown as a reference. SYN: synergy site. RGD: arg-gly-asp.

Figure 2: Force and COM extension over time plotted over punctual stress at R1374/1379 of the synergy site for A) 10nm/ns
 wildtype $\alpha_5\beta_1$ -FN, B) 1nm/ns wildtype $\alpha_5\beta_1$ -FN, C) 10nm/ns R1374/9A $\alpha_5\beta_1$ -FN, and D) 1nm/ns R1374/9A $\alpha_5\beta_1$ -FN.
 Positions (i), (ii), and (iii) correspond to the time at the peak force, local minimum, and final frame, respectively.

Montes et al.

Figure 3: Force on $\alpha_5\beta_1$ -FN and radius of gyration of α_5 and β_1 head for the 1nm/ns runs for the A) wildtype and B) mutant. Positions (i), (ii), and (iii) correspond to the time at the peak force, local minimum, and final frame. The four shown frames from the simulation correspond to the first frame, (i) peak force, (ii) local minimum, and (iii) final frame for C) wildtype and D) mutant.

Figure 4: A) Cryo-EM structure $\alpha_5\beta_1$ -FN9-10. Small restraints were placed on D603, E445, and D1348 in the x and y directions to mimic the respective continuing structures of integrin and FN. θ_{int} was defined the angle between the principal axes of inertia of α_5 and β_1 , respectively. Similarly, θ_{FN} was defined as the angle between the principal axes of inertia of FN9 and FN10, respectively. Dashed lines are hand-drawn and indicate an approximation of the principal axes. SYN: synergy site. B) Superposition of the wildtype (blue) and mutant (orange) during the first and last frames of the respective 250ns simulations. C) Nonbounded interaction energy between the synergy site and $\alpha_5\beta_1$ integrin for wildtype and mutant. D) Minimum distance between residue 1379 (FN9) and D154 (α_5) for wildtype and mutant. E) Violin plot of FN9-10 angle for last 50ns of 250ns simulation (WT = $151.4 \pm 4.9^\circ$, R1374/9A = $151.4 \pm 2.2^\circ$, $p = 0.98$). F) Violin plot of $\alpha_5\beta_1$ angle for last 50ns of 250ns simulation (WT = $53.9 \pm 4.3^\circ$, R1374/9A = $46.7 \pm 3.8^\circ$, $p < 0.0001$).

Figure 5: A) Schematic of whole-cell interface model that assumes that integrin behaves as a spring that is stretched due to cell contraction. B) Catch bond model: $\alpha_5\beta_1$ -FN bond lifetime versus applied force for wildtype (adapted from (38, 39)). C) Concentration over time of wildtype and mutant $\alpha_5\beta_1$ -FN. D) Force over time of wildtype and mutant $\alpha_5\beta_1$ -FN. E) Frames at times 2, 4, and 6s indicating the concentration of $\alpha_5\beta_1$ -FN bonds across the cell-substrate interface during a 200Pa uniform contraction. F) Frames at times 2, 4, and 6s indicating the distribution of $\alpha_5\beta_1$ -FN bond force across the cell-substrate interface during a 200Pa uniform contraction.

Figure 6: Proposed model for synergy site clip engagement leading to α_5 deformation during mechanosensing while RGD acts as a pivot for FN10. In this model, force transmits across the clip, stretching α_5 . The additional energetic barrier provided by the clip could afford $\alpha_5\beta_1$ -FN greater resistance to unbinding. The rigidity of β_1 relative to α_5 may allow for force transmission across the membrane and towards the mechanosensitive cytoskeletal protein, talin, leading to downstream mechanosignaling.

404 AUTHOR CONTRIBUTIONS

405 A.R.M., A.B.T., and M.R.K.M. conceptualized and designed the research. A.R.M., A.B., and W.W. performed the research and
406 analyzed data. A.R.M. wrote the manuscript. G.D.O., A.B.T., and M.R.K.M. supervised the research and edited the manuscript.

407 ACKNOWLEDGMENTS

408 This research used Expanse at San Diego Supercomputer Center through allocation MCB100146 from Advanced Cyberin-
409 frastructure Coordination Ecosystem: Services & Support (ACCESS) super-computing facilities, supported by the National
410 Science Foundation (NSF) (Grant Nos. 2138259, 2138286, 2138307, 2137603, and 2138296). We also acknowledge the
411 additional allocation, BIO230214 for use of Expanse as well as the Negishi Community Cluster managed by the Rosen Center
412 for Advanced Computing. A.R.M. was supported by the Ford Predoctoral Fellowship, UC Berkeley College of Engineering
413 Robert N. Noyce Fellowship, and Hearts to Humanity Eternal Research Fellowship. A.B. was supported by the National Institute
414 of Health Maximizing Access to Research Careers T34 Award. W.W. was supported by the NSF Research Experience for
415 Undergraduates via the Transfer-to-Excellence Program at University of California, Berkeley. A.B.T was supported by the UC
416 Berkeley Miller Institute for Basic Research in Science. We thank members of the Molecular Cell Biomechanics and Berkeley
417 Biomechanics Labs for fruitful discussions that led to the improvement of this manuscript. Special thank you to Mohammad
418 Khavani for his suggestions to improve the molecular dynamics simulations.

419 DECLARATION OF INTERESTS

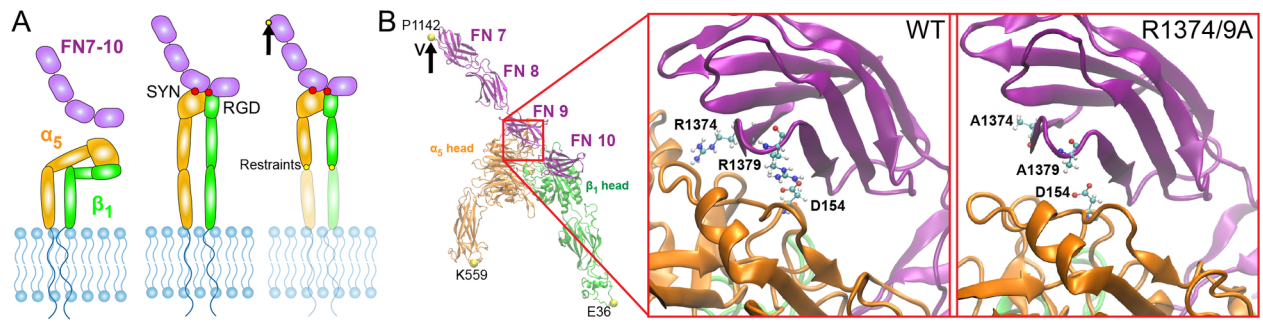
420 The authors declare no competing interests.

REFERENCES

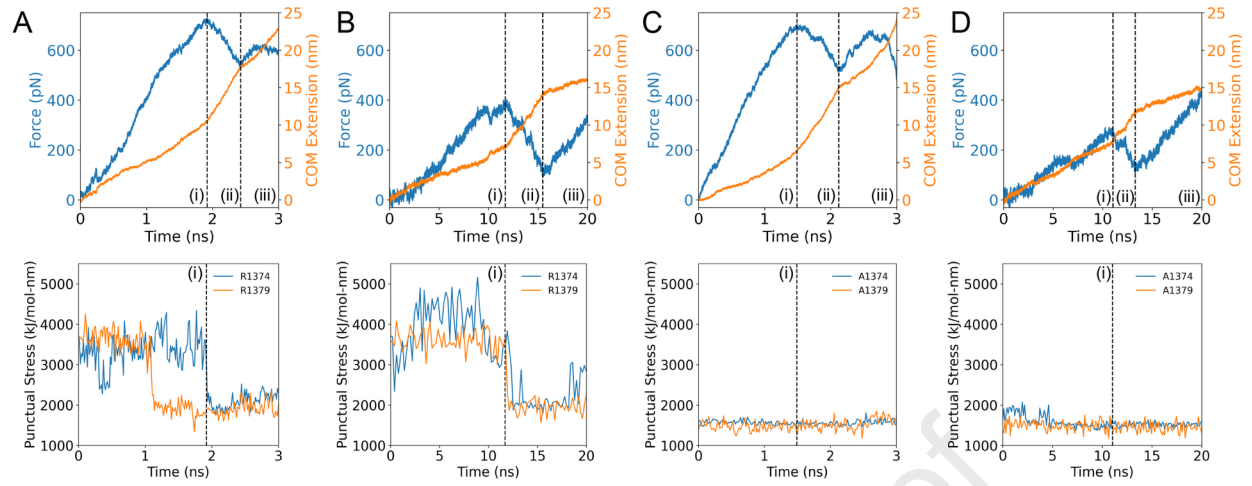
- 421
- 422 1. Damiano, J. S., A. E. Cress, L. A. Hazlehurst, A. A. Shtil, and W. S. Dalton, 1999. Cell adhesion mediated drug resistance
423 (CAM-DR): role of integrins and resistance to apoptosis in human myeloma cell lines. *Blood, the Journal of the American*
424 *Society of Hematology* 93:1658–1667.
- 425 2. Bachmann, M., S. Kukkurainen, V. P. Hytönen, and B. Wehrle-Haller, 2019. Cell adhesion by integrins. *Physiological*
426 *reviews* 99:1655–1699.
- 427 3. Lee, M. H., P. Ducheyne, L. Lynch, D. Boettiger, and R. J. Composto, 2006. Effect of biomaterial surface properties on
428 fibronectin- $\alpha 5\beta 1$ integrin interaction and cellular attachment. *Biomaterials* 27:1907–1916.
- 429 4. Hynes, R. O., 2002. Integrins: bidirectional, allosteric signaling machines. *cell* 110:673–687.
- 430 5. Ross, T. D., B. G. Coon, S. Yun, N. Baeyens, K. Tanaka, M. Ouyang, and M. A. Schwartz, 2013. Integrins in
431 mechanotransduction. *Current opinion in cell biology* 25:613–618.
- 432 6. Cutler, S. M., and A. J. García, 2003. Engineering cell adhesive surfaces that direct integrin $\alpha 5\beta 1$ binding using a
433 recombinant fragment of fibronectin. *Biomaterials* 24:1759–1770.
- 434 7. Scheiblin, D. A., J. Gao, J. L. Caplan, V. N. Simirskii, K. J. Czymmek, R. T. Mathias, and M. K. Duncan, 2014. Beta-1
435 integrin is important for the structural maintenance and homeostasis of differentiating fiber cells. *The international journal*
436 *of biochemistry & cell biology* 50:132–145.
- 437 8. Humphrey, J. D., E. R. Dufresne, and M. A. Schwartz, 2014. Mechanotransduction and extracellular matrix homeostasis.
438 *Nature reviews Molecular cell biology* 15:802–812.
- 439 9. Benito-Jardón, M., S. Klapproth, I. Gimeno-LLuch, T. Petzold, M. Bharadwaj, D. J. Müller, G. Zuchriegel, C. A. Reichel,
440 and M. Costell, 2017. The fibronectin synergy site re-enforces cell adhesion and mediates a crosstalk between integrin
441 classes. *Elife* 6:e22264.
- 442 10. Hou, J., D. Yan, Y. Liu, P. Huang, and H. Cui, 2020. The roles of integrin $\alpha 5\beta 1$ in human cancer. *Oncotargets and therapy*
443 13329–13344.
- 444 11. Zhao, X.-K., Y. Cheng, M. Liang Cheng, L. Yu, M. Mu, H. Li, Y. Liu, B. Zhang, Y. Yao, H. Guo, et al., 2016. Focal
445 adhesion kinase regulates fibroblast migration via integrin beta-1 and plays a central role in fibrosis. *Scientific reports*
446 6:19276.
- 447 12. Cao, L., J. Nicosia, J. Larouche, Y. Zhang, H. Bachman, A. C. Brown, L. Holmgren, and T. H. Barker, 2017. Detection of
448 an integrin-binding mechanoswitch within fibronectin during tissue formation and fibrosis. *ACS nano* 11:7110–7117.
- 449 13. Schumacher, S., D. Dedden, R. V. Nunez, K. Matoba, J. Takagi, C. Biertümpfel, and N. Mizuno, 2021. Structural insights
450 into integrin $\alpha 5\beta 1$ opening by fibronectin ligand. *Science Advances* 7:eabe9716.
- 451 14. Kechagia, J. Z., J. Ivaska, and P. Roca-Cusachs, 2019. Integrins as biomechanical sensors of the microenvironment. *Nature*
452 *Reviews Molecular Cell Biology* 20:457–473.
- 453 15. Schaffner, F., A. M. Ray, and M. Dontenwill, 2013. Integrin $\alpha 5\beta 1$, the fibronectin receptor, as a pertinent therapeutic target
454 in solid tumors. *Cancers* 5:27–47.
- 455 16. Cox, D., M. Brennan, and N. Moran, 2010. Integrins as therapeutic targets: lessons and opportunities. *Nature reviews*
456 *Drug discovery* 9:804–820.
- 457 17. Kong, F., A. J. García, A. P. Mould, M. J. Humphries, and C. Zhu, 2009. Demonstration of catch bonds between an integrin
458 and its ligand. *Journal of Cell Biology* 185:1275–1284.
- 459 18. Strohmeyer, N., M. Bharadwaj, M. Costell, R. Fässler, and D. J. Müller, 2017. Fibronectin-bound $\alpha 5\beta 1$ integrins sense
460 load and signal to reinforce adhesion in less than a second. *Nature Materials* 16:1262–1270.
- 461 19. Dansuk, K. C., and S. Keten, 2021. Self-strengthening biphasic nanoparticle assemblies with intrinsic catch bonds. *Nature*
462 *communications* 12:85.

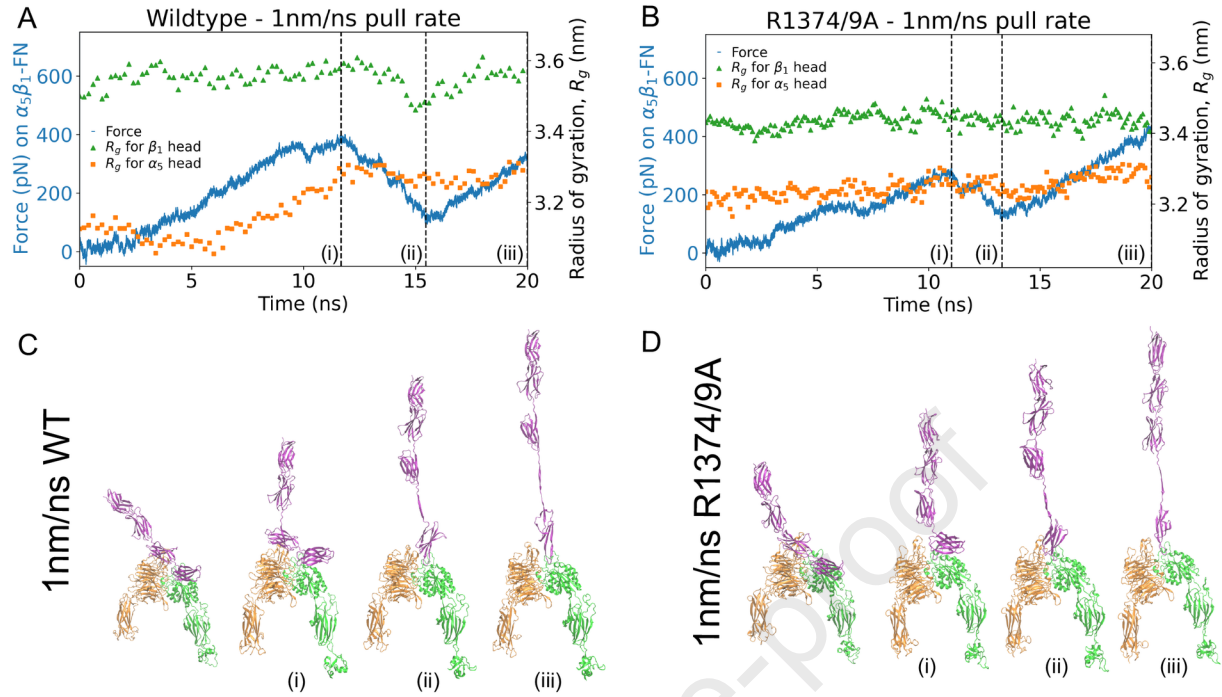
- 463 20. Dansuk, K. C., S. Pal, and S. Keten, 2023. A catch bond mechanism with looped adhesive tethers for self-strengthening
464 materials. *Communications Materials* 4:60.
- 465 21. Yuan, Z., X. Duan, X. Su, Z. Tian, A. Jiang, Z. Wan, H. Wang, P. Wei, B. Zhao, X. Liu, et al., 2023. Catch bond-inspired
466 hydrogels with repeatable and loading rate-sensitive specific adhesion. *Bioactive Materials* 21:566–575.
- 467 22. Kulke, M., and W. Langel, 2020. Molecular dynamics simulations to the bidirectional adhesion signaling pathway of
468 integrin $\alpha V\beta 3$. *Proteins: Structure, Function, and Bioinformatics* 88:679–688.
- 469 23. Montes, A. R., G. Gutierrez, A. Buganza Tepole, and M. R. K. Mofrad, 2023. Multiscale computational framework to
470 investigate integrin mechanosensing and cell adhesion. *Journal of Applied Physics* 134:114702.
- 471 24. Friedland, J. C., M. H. Lee, and D. Boettiger, 2009. Mechanically activated integrin switch controls $\alpha 5\beta 1$ function. *Science*
472 323:642–644.
- 473 25. Chang, A. C., A. H. Mekhdjian, M. Morimatsu, A. K. Denisin, B. L. Pruitt, and A. R. Dunn, 2016. Single molecule force
474 measurements in living cells reveal a minimally tensioned integrin state. *ACS nano* 10:10745–10752.
- 475 26. Abraham, M. J., T. Murtola, R. Schulz, S. Páll, J. C. Smith, B. Hess, and E. Lindahl, 2015. GROMACS: High performance
476 molecular simulations through multi-level parallelism from laptops to supercomputers. *SoftwareX* 1:19–25.
- 477 27. Schrödinger, L., 2015. The PyMOL Molecular Graphics System, Version 1.8.
- 478 28. Webb, B., and A. Sali, 2016. Comparative protein structure modeling using MODELLER. *Current protocols in*
479 *bioinformatics* 54:5–6.
- 480 29. Humphrey, W., A. Dalke, and K. Schulten, 1996. VMD: visual molecular dynamics. *Journal of molecular graphics*
481 14:33–38.
- 482 30. Costescu, B. I., and F. Gräter, 2013. Time-resolved force distribution analysis. *BMC biophysics* 6:1–5.
- 483 31. Tong, D., N. Soley, R. Kolasangiani, M. A. Schwartz, and T. C. Bidone, 2023. Integrin $\alpha IIb\beta 3$ intermediates: From
484 molecular dynamics to adhesion assembly. *Biophysical Journal* 122:533–543.
- 485 32. Luo, Q., D. Kuang, B. Zhang, and G. Song, 2016. Cell stiffness determined by atomic force microscopy and its correlation
486 with cell motility. *Biochimica et Biophysica Acta (BBA)-General Subjects* 1860:1953–1960.
- 487 33. Schierbaum, N., J. Rheinlaender, and T. E. Schäffer, 2019. Combined atomic force microscopy (AFM) and traction force
488 microscopy (TFM) reveals a correlation between viscoelastic material properties and contractile prestress of living cells.
489 *Soft Matter* 15:1721–1729.
- 490 34. Chen, C., J. Xie, L. Deng, and L. Yang, 2014. Substrate stiffness together with soluble factors affects chondrocyte
491 mechanoresponses. *ACS applied materials & interfaces* 6:16106–16116.
- 492 35. Guo, Y., S. Calve, and A. B. Tepole, 2022. Multiscale mechanobiology: Coupling models of adhesion kinetics and nonlinear
493 tissue mechanics. *Biophysical Journal* 121:525–539.
- 494 36. Cheng, B., W. Wan, G. Huang, Y. Li, G. M. Genin, M. R. Mofrad, T. J. Lu, F. Xu, and M. Lin, 2020. Nanoscale integrin
495 cluster dynamics controls cellular mechanosensing via FAKY397 phosphorylation. *Science advances* 6:eaax1909.
- 496 37. Bell, G. I., 1978. Models for the specific adhesion of cells to cells: a theoretical framework for adhesion mediated by
497 reversible bonds between cell surface molecules. *Science* 200:618–627.
- 498 38. Bidone, T. C., A. V. Skeeters, P. W. Oakes, and G. A. Voth, 2019. Multiscale model of integrin adhesion assembly. *PLOS*
499 *Computational Biology* 15:e1007077.
- 500 39. Takagi, J., K. Strokovich, T. A. Springer, and T. Walz, 2003. Structure of integrin $\alpha 5\beta 1$ in complex with fibronectin. *The*
501 *EMBO journal* 22:4607–4615.
- 502 40. Gaudet, C., W. A. Marganski, S. Kim, C. T. Brown, V. Gunderia, M. Dembo, and J. Y. Wong, 2003. Influence of type I
503 collagen surface density on fibroblast spreading, motility, and contractility. *Biophysical journal* 85:3329–3335.

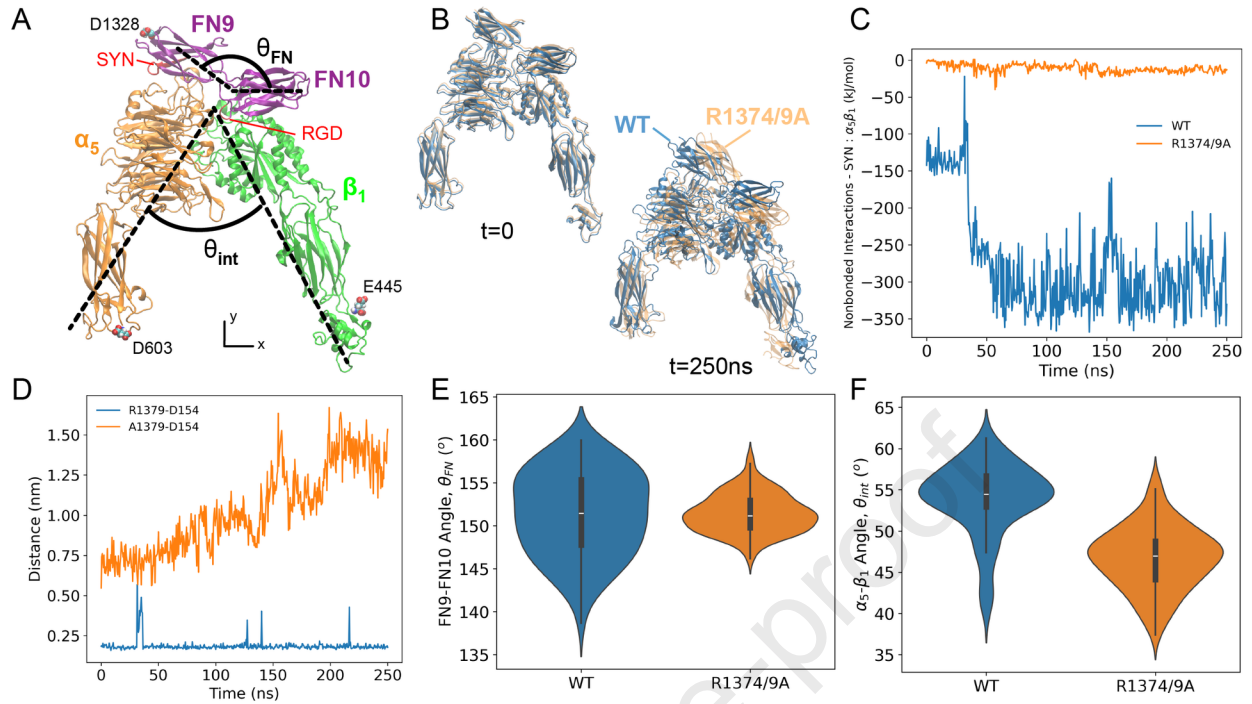
- 504 41. Neurohr, G. E., and A. Amon, 2020. Relevance and regulation of cell density. *Trends in cell biology* 30:213–225.
- 505 42. Brochu, T., and R. Bridson, 2009. Robust topological operations for dynamic explicit surfaces. *SIAM Journal on Scientific*
506 *Computing* 31:2472–2493.
- 507 43. Li, F., S. D. Redick, H. P. Erickson, and V. T. Moy, 2003. Force measurements of the $\alpha5\beta1$ integrin–fibronectin interaction.
508 *Biophysical journal* 84:1252–1262.
- 509 44. Chen, W., J. Lou, J. Hsin, K. Schulten, S. C. Harvey, and C. Zhu, 2011. Molecular dynamics simulations of forced
510 unbending of integrin $\alpha V\beta3$. *PLoS computational biology* 7:e1001086.
- 511 45. Aota, S.-i., M. Nomizu, and K. M. Yamada, 1994. The short amino acid sequence Pro-His-Ser-Arg-Asn in human
512 fibronectin enhances cell-adhesive function. *Journal of Biological Chemistry* 269:24756–24761.
- 513 46. Redick, S. D., D. L. Settles, G. Briscoe, and H. P. Erickson, 2000. Defining fibronectin’s cell adhesion synergy site by
514 site-directed mutagenesis. *The Journal of cell biology* 149:521–527.
- 515 47. García, A. J., J. E. Schwarzbauer, and D. Boettiger, 2002. Distinct activation states of $\alpha5\beta1$ integrin show differential
516 binding to RGD and synergy domains of fibronectin. *Biochemistry* 41:9063–9069.
- 517 48. Tan, S. J., A. C. Chang, S. M. Anderson, C. M. Miller, L. S. Prah, D. J. Odde, and A. R. Dunn, 2020. Regulation and
518 dynamics of force transmission at individual cell-matrix adhesion bonds. *Science Advances* 6:eaax0317.
- 519 49. Zhou, D. W., M. A. Fernández-Yagüe, E. N. Holland, A. F. García, N. S. Castro, E. B. O’Neill, J. Eyckmans, C. S.
520 Chen, J. Fu, D. D. Schlaepfer, et al., 2021. Force-FAK signaling coupling at individual focal adhesions coordinates
521 mechanosensing and microtissue repair. *Nature communications* 12:2359.
- 522 50. Holland, E. N., M. A. Fernández-Yagüe, D. W. Zhou, E. B. O’Neill, A. U. Woodfolk, A. Mora-Boza, J. Fu, D. D. Schlaepfer,
523 and A. J. García, 2024. FAK, vinculin, and talin control mechanosensitive YAP nuclear localization. *Biomaterials*
524 308:122542.
- 525 51. Jahed, Z., H. Shams, M. Mehrbod, and M. R. Mofrad, 2014. Mechanotransduction pathways linking the extracellular
526 matrix to the nucleus. *International review of cell and molecular biology* 310:171–220.
- 527 52. Shattil, S. J., C. Kim, and M. H. Ginsberg, 2010. The final steps of integrin activation: the end game. *Nature reviews*
528 *Molecular cell biology* 11:288–300.
- 529 53. Takagi, J., B. M. Petre, T. Walz, and T. A. Springer, 2002. Global conformational rearrangements in integrin extracellular
530 domains in outside-in and inside-out signaling. *Cell* 110:599–611.
- 531 54. Driscoll, T. P., T. C. Bidone, S. J. Ahn, A. Yu, A. Groisman, G. A. Voth, and M. A. Schwartz, 2021. Integrin-based
532 mechanosensing through conformational deformation. *Biophysical journal* 120:4349–4359.
- 533 55. Mehrbod, M., S. Trisno, and M. R. Mofrad, 2013. On the activation of integrin $\alpha IIB\beta3$: outside-in and inside-out pathways.
534 *Biophysical journal* 105:1304–1315.
- 535 56. Su, S., Y. Ling, Y. Fang, and J. Wu, 2022. Force-enhanced biophysical connectivity of platelet $\beta3$ integrin signaling
536 through Talin is predicted by steered molecular dynamics simulations. *Scientific reports* 12:4605.
- 537 57. Bidone, T. C., A. Polley, J. Jin, T. Driscoll, D. V. Iwamoto, D. A. Calderwood, M. A. Schwartz, and G. A. Voth, 2019.
538 Coarse-grained simulation of full-length integrin activation. *Biophysical journal* 116:1000–1010.
- 539 58. Ji, Y., Y. Fang, and J. Wu, 2022. Tension Enhances the Binding Affinity of $\beta1$ Integrin by Clamping Talin Tightly: An
540 Insight from Steered Molecular Dynamics Simulations. *Journal of Chemical Information and Modeling* 62:5688–5698.
- 541 59. Pan, D., and Y. Song, 2010. Role of altered sialylation of the I-like domain of $\beta1$ integrin in the binding of fibronectin to
542 $\beta1$ integrin: thermodynamics and conformational analyses. *Biophysical journal* 99:208–217.

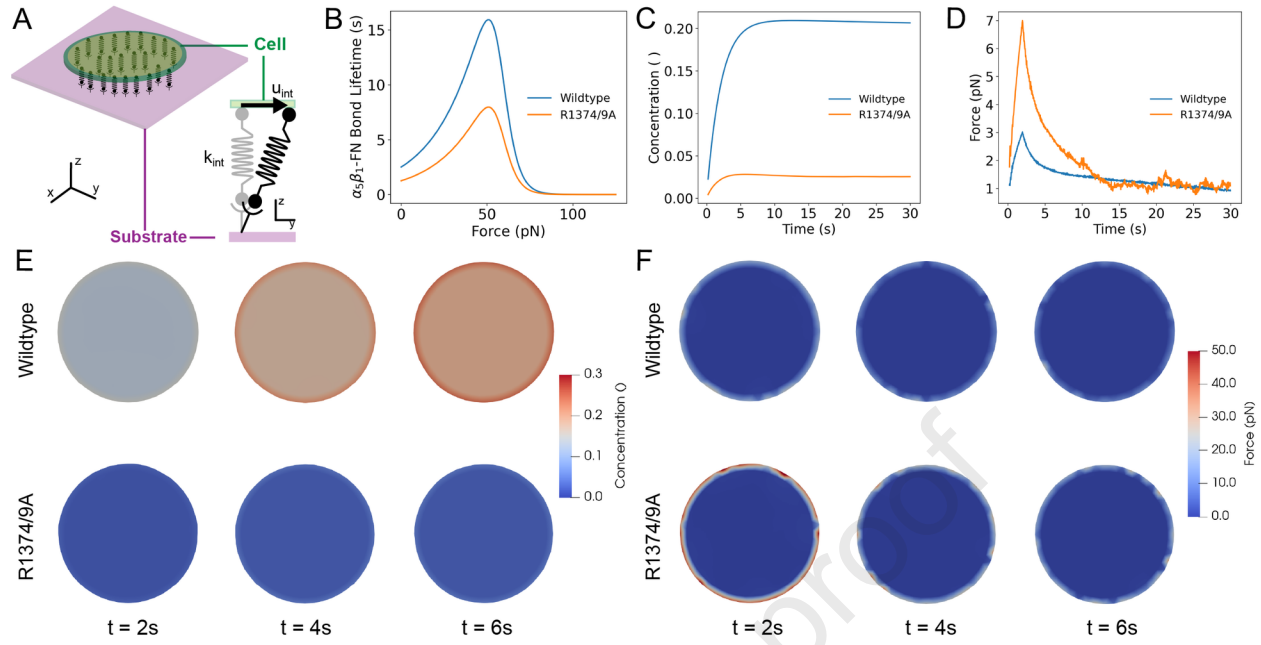


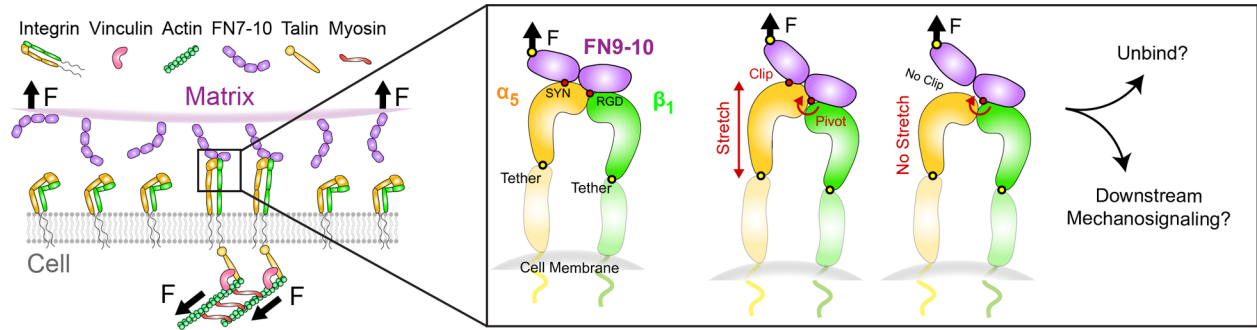
Journal Pre-proof











Journal Pre-proof